UNIVERSITY OF
BATH

University of Bath

Mapping the radio sky with an interferometric network of low-frequency radio receivers

Andrew Mezentsev[1] and Martin Füllekrug[1]

[1]   The structure of the 100 kHz radio sky is determined with two interferometric networks of 10 radio receivers which are distributed over local areas of $\sim 1 \times 1$ km^2 and $\sim 10 \times 10$ km^2. The radio waves arrive at individual receiver pairs with small time differences which are used to determine the arrival direction of the electromagnetic waves including both the bearing and the elevation angle. The results show that the major part of the 100 kHz radio wave energy comes from the horizon at bearings which are consistent with known locations of Long Range Navigation (LORAN) transmitters. Some part of the radio wave energy arrives from the sky at elevation angles which are consistent with the first and second sky hop waves of LORAN transmissions. A minor part of the 100 kHz radio wave energy comes from lightning discharges at distances up to ~ 1000 km with bearings which are consistent with lightning locations reported by the arrival time difference (ATD) lightning detection network of the UK Met Office. The angular resolution for mapping the radio sky depends on the network geometry, the instrumental timing accuracy, and on the signal-to-noise ratio of the radio waves. The resulting angular resolution of the interferometric networks used in this study is $\sim 1°$ in bearing at zero elevation and several degrees in elevation.

1.   Introduction

[2]   It was recently found that the area above thunderclouds is the source of diverse electromagnetic phenomena. For example, it was reported that sprites [e.g., *Füllekrug et al.*, 2001; *Cummer and Füllekrug*, 2001; *Pasko et al.*, 1998; *Cummer and Inan*, 1997], gigantic jets [*Cummer et al.*, 2009], and upward electron beams [e.g., *Füllekrug et al.*, 2011, 2010; *Roussel-Dupré et al.*, 1998] exhibit distinct electromagnetic signatures. In the future, it may be also possible to detect the radiation from other lightning-related events, such as streamer discharges above thunderclouds [*Qin et al.*, 2012], lightning-induced particle precipitation [e.g., *Gemelos et al.*, 2009; *Rodger et al.*, 2007; *Inan et al.*, 2007], or more generally energetic charged particles above thunderclouds [*Füllekrug et al.*, 2013]. The radio emissions from electromagnetic phenomena above thunderclouds contain valuable information about the source, e.g., the location, intensity, and the spatial and temporal development of the source.

[3]   Numerous methods have been developed to locate lightning discharges on the ground. For example, arrival time difference analysis [e.g., *Lee*, 1986; *Lewis et al.*, 1960], direction finding [*Cummins et al.*, 1998], time of group arrival [*Dowden et al.*, 2002], or matching waveform tables [*Said et al.*, 2010]. The corresponding radio receiver networks operate on the global scale $\sim 10^3$–10^4 km [e.g., *Rodger et al.*, 2006; *Sato and Fukunishi*, 2003; *Füllekrug and Constable*, 2000], on the mesoscale $\sim 10^2$–10^3 km [e.g., *Shao et al.*, 2006; *Betz et al.*, 2004; *Cummins et al.*, 1998], and on the regional scale $\sim 10^1$–10^2 km [e.g., *Krehbiel et al.*, 2008].

[4]   However, networks operating at low frequencies from ~ 30–300 kHz and on the local scale $\sim 10^0$–10^1 km have been little studied. This contribution explores the opportunities arising from such local scale interferometric networks to determine the detection and location of electromagnetic radiation sources above thunderclouds. The study focuses in particular on the pulsed 100 kHz radio emissions from Long Range Navigation (LORAN) transmitters which are extremely stable and very well documented [*Füllekrug*, 2010; *United States Coast Guard*, 1994]. This contribution presents the underlying theory to determine the arrival direction of the electromagnetic waves, including both the bearing and the elevation angle. The theory is validated by measurements with interferometric networks on two different local scales of $\sim 1 \times 1$ km^2 and $\sim 10 \times 10$ km^2.

2.   Theory

[5]   Consider a network of N radio receivers which form $(N-1)$ linearly independent pairs of instruments. Thus, a

---

[1]Centre for Space, Atmospheric and Oceanic Science, Department of Electronic and Electrical Engineering, University of Bath, Bath, UK.

Corresponding author: A. Mezentsev, Centre for Space, Atmospheric and Oceanic Science, Department of Electronic and Electrical Engineering, University of Bath, Bath, BA2 7AY, UK. (andrew.mezentsev@gmail.com)

Table 1. Charmy Down Network Coordinates[a]

No.	Lat (°N)	Lon (°W)	Height (m)
01	51.42974	2.35374	208
02	51.43113	2.35109	208
03	51.43120	2.33875	207
04	51.42765	2.34259	206
05	51.42875	2.34571	206
06	51.42968	2.34865	210
07	51.42459	2.34439	202
08	51.42445	2.34111	205
09	51.42704	2.33613	210
10	51.42633	2.33908	209

[a]Geographic coordinates of the 10 radio receivers which form the interferometric network on Charmy Down airfield near Bath in South West England of the UK. The locations of the instruments are known with an accuracy better than ~4 m.

network of 10 instruments forms 9 independent pairs. The kth pair of instruments is characterized by its relative location, expressed in Cartesian coordinates by its pair vector

$$\mathbf{b_k} = (x_i - x_j, y_i - y_j, z_i - z_j), \tag{1}$$

where i and j are the instruments of the kth pair.

[6] The unit vector pointing to the source is

$$\mathbf{r} = (\cos\varphi\cos\vartheta, \sin\varphi\cos\vartheta, \sin\vartheta), \tag{2}$$

where the bearing φ counts clockwise from the geographic north and the elevation angle ϑ counts from the horizon upward to the zenith. The source detection is based on the observation of arrival time differences Δt_k which correspond to observed path length differences Δl_k by use of the speed of light c

$$\Delta l_k = c\Delta t_k. \tag{3}$$

[7] When the source is far away from the network, i.e., the distance to the source R is much larger than a characteristic average baseline b_a, e.g., $R/b_a > 100$, the theoretical time difference Δt_k^* is calculated from the scalar product between the source vector $\mathbf{r}$ and the pair vector $\mathbf{b_k}$

$$\Delta t_k^*(\varphi, \vartheta) = \frac{1}{c}(\mathbf{r}, \mathbf{b_k}). \tag{4}$$

The observed and theoretical time differences define a mean square deviation

$$J(\varphi, \theta) = \sum_{k=1}^{N-1} \left(\Delta t_k - \Delta t_k^*(\varphi, \vartheta)\right)^2, \tag{5}$$

where the summation extends over $(N - 1)$ independent receiver pairs. The best solution (φ_0, ϑ_0) for the bearing and the elevation angle minimizes the deviation

$$(\varphi_0, \vartheta_0) = \arg\min_{(\varphi, \vartheta) \in \mathcal{U}} J(\varphi, \vartheta), \tag{6}$$

where $\mathcal{U}$ is the upper hemisphere of a unit sphere.

[8] When the source is closer, e.g., $R/b_a < 100$, the distance between the source and the network needs to be taken into account. The theoretical time difference Δt_k^* in this case is

$$\Delta t_k^*(\varphi_i, \vartheta_i, R_i) = \frac{1}{c}(R_i - R_j), \tag{7}$$

where R_i is the distance between the source and the ith instrument and R_j is the distance between the source and the

Table 2. Rustrel Network Coordinates[a]

No.	Lat (°N)	Lon (°E)	Height (m)
01	43.94527	5.53473	783
02	43.98687	5.45624	1115
03	44.02913	5.46567	1004
04	44.01972	5.54064	841
05	43.98422	5.48918	1211
06	44.00142	5.48770	1092
07	43.94092	5.48386	1009

[a]Geographic coordinates of the seven radio receivers which form the interferometric network on Plateau d'Albion near Rustrel in Southern France.

jth instrument. R_j can be calculated with the cosine theorem, such that

$$\Delta t_k^*(\varphi_i, \vartheta_i, R_i) = \frac{1}{c}\left(R_i - \sqrt{R_i^2 + b_k^2 - 2R_i(\mathbf{r}, \mathbf{b_k})}\right). \tag{8}$$

The best solution $(\varphi_0, \vartheta_0, R_0)$ minimizes the mean square deviation with respect to the bearing, elevation angle and distance

$$(\varphi_0, \vartheta_0, R_0) = \arg\min_{(\varphi, \vartheta, R) \in \mathcal{U} \otimes \mathcal{R}} J(\varphi, \vartheta, R), \tag{9}$$

where $\mathcal{R} = (0, 100b_a)$.

3. Experiment

[9] An interferometric network of radio receivers was deployed on an old airfield at Charmy Down near Bath in South West England. Daytime recordings during the time interval from 14:36:45–14:56:45 UTC on 13 May 2011 were collected. The network consists of 10 wideband digital low-frequency radio receivers which record vertical electric field strengths in the frequency range from ~4 Hz to ~400 kHz with a sampling frequency of 1 MHz, an amplitude resolution of ~35 μV/m and a relative timing accuracy of ~12 ns provided by the GPS clock [*Füllekrug*, 2010]. The radio receivers are distributed over an area of ~1 × 1
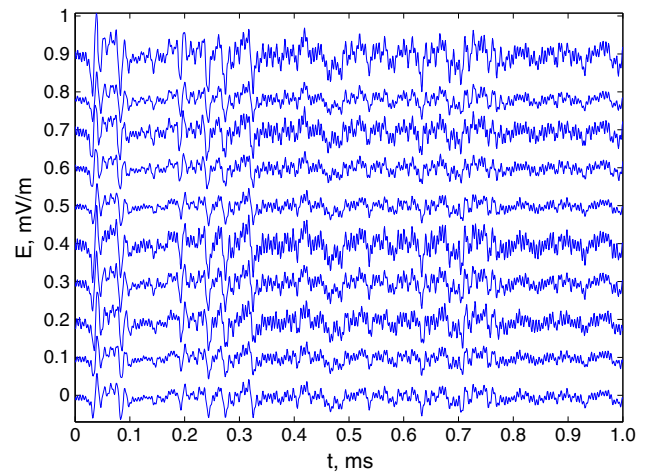

Figure 1. Vertical electric field recordings in the frequency range from ~4 Hz–400 kHz with 10 radio receivers. An offset of 100 mV/m is added consecutively to the recordings. All recordings exhibit highly coherent waveforms with small time delays which reflect the propagation of electromagnetic waves across the network.

Table 3. LORAN Transmitters With Respect to Charmy Down Network[a]

Name	Lat (°N)	Lon (°W)	φ (°)	$\overline{\varphi}$ (°)	d (km)	Δt_{gsd} (μs)	Δt_{gsn} (μs)
LSY	49.1486	−1.5047	166.29	166	260	88	187
ANT	54.9112	−3.2872	351.22	351	393	60	131
SST	43.7397	−1.3804	174.74	175	858	28	62
RNT	54.8083	8.2935	58.00	60	804	30	66

[a]Geographic coordinates of the four LORAN transmitters Lessay (LSY), France, Soustons (SST), France, Anthorn (ANT), UK, and Rantum (RNT), Germany. The expected bearing φ and the average observed bearing $\overline{\varphi}$ of the LORAN transmitters observed with the network at Charmy Down agree within ∼1°. The distances d between the LORAN transmitters and the network enable the determination of the corresponding arrival time differences between the ground wave and the sky wave (Δt_{gs}) which are calculated here for an ionospheric height of 60 km for daytime (Δt_{gsd}) and 90 km for nighttime (Δt_{gsn}).

km^2 (Table 1). The shortest distance between instruments is ∼200 m and the largest distance between instruments is ∼1260 m.

[10] For the nighttime recordings, the other network of seven instruments was deployed in Southern France near Rustrel (44.0°N, 5.5°E) on 11 August 2011 over the area of ∼10 × 10 km^2 (Table 2). The shortest baseline of this network is ∼1.9 km and the longest baseline is ∼10 km.

[11] The locations of the instruments are determined by Global Positioning Satellites (GPS) with an accuracy better than ∼4 m. The irregular spacing between the instruments results from logistic constraints and accessibility to the area. The waveforms recorded by the Charmy Down network are highly coherent (Figure 1). The small time differences reflect the propagation of electromagnetic waves across the network. These time differences are used to determine the arrival direction including both the bearing and elevation angle of the arriving electromagnetic energy.

[12] The individual timings of all instruments of the Charmy Down network are synchronized to each other by use of the nearest LORAN transmitter at Lessay in northern France which is ∼260 km away from Charmy Down. Similarly, the individual timings of all instruments of the Rustrel network are synchronized to each other by use of the nearest LORAN transmitter at Soustons in western France which is ∼556 km away from Rustrel.

[13] LORAN is a terrestrial radio navigation system which operates at a center frequency of 100 kHz with a protected bandwidth of ±10 kHz [*Füllekrug et al.*, 2009; *United States Coast Guard*, 1994]. LORAN transmitters are mainly used for marine navigation but also distribute atomic time with an accuracy ∼<20 ns [*Füllekrug*, 2010].

[14] The Northwest European LORAN System (NELS) consists of several sets of transmitters (chains) with different coverage areas. Each transmitter emits a group of eight ∼200 μs long pulses which are separated by 1 ms. These pulse groups are repeated with a Group Repetition Interval

(GRI) which is specific for each chain. Some transmitters participate in different chains. Four LORAN transmitters can be observed at Charmy Down, namely, Lessay (LSY), Soustons (SST), Anthorn (ANT), and Rantum (RNT) (Table 3). These four transmitters form the Lessay chain with a GRI of 67,310 μs. LSY and RNT also participate in the Sylt chain with a GRI of 74,990 μs, which leads to occasional but deterministic overlaps between LSY transmissions as part of the Sylt chain and ANT, SST, RNT transmissions as part of the Lessay chain. Similar overlaps occur between RNT transmissions as part of the Sylt chain and LSY, ANT, SST transmissions as part of the Lessay chain. These transmission overlaps cause an "interchain" interference which is discussed in more detail in section 5. The same four LORAN transmitters can be observed at Rustrel, except that the RNT transmitter was off during the night of the experiment due to maintenance works (Table 4).

4. Solution Accuracy and Network Resolution

[15] The waveforms of the sources recorded by the network demonstrate specific time delays between different instruments. The bearing and elevation to the source can be found by substituting these time delays into (5) and subsequent minimization (6). Thus, the accuracy of the solution is defined by three factors which can be analyzed separately: (i) the accuracy of the time differences, (ii) the accuracy of the minimization procedure, and (iii) the network resolution.

[16] 1. The accuracy of the time differences depends on the timing accuracy of the GPS clocks (∼12 ns), the accuracy of the network synchronization (∼100 ns for the Charmy Down network and ∼300 ns for the Rustrel network), and on the signal-to-noise ratio of a source. All of the above depend on the wavelength to baseline length ratio. For the Charmy Down experiment, the overall accuracy level of the time differences is estimated to be ∼100 ns by use of the LORAN signals. For the Rustrel experiment, the over-

Table 4. LORAN Transmitters With Respect to Southern France Network[a]

Name	φ (°)	$\overline{\varphi}$ (°)	ϑ_1 (°)	$\overline{\vartheta_1}$ (°)	ϑ_2 (°)	$\overline{\vartheta_2}$ (°)	d (km)	Δt_{gs1} (μs)	Δt_{gs2} (μs)
LSY	319.58	320	13.86	15	26.27	27	790	70	272
SST	270.04	270	19.06	21	34.64	35	556	99	370
ANT	335.67	335	7.90	8	15.50	13	1375	41	161

[a]The expected bearing φ and the average observed bearing $\overline{\varphi}$ of the LORAN transmitters observed with the network in Southern France agree within ∼1°. The expected elevation angle for the first hop sky wave ϑ_1 and the average observed elevation angle $\overline{\vartheta}_1$ agree within ∼2°. The expected elevation angle for the second hop sky wave ϑ_2 and the average observed elevation angle $\overline{\vartheta}_2$ also agree within ∼2°. The distances d between the LORAN transmitters (LSY, SST, and ANT) and the network in Southern France enable a determination of the arrival time differences between the ground wave and the first hop sky wave Δt_{gs1} and between the ground wave and the second hop sky wave Δt_{gs2} which are calculated here for an ionospheric height of 90 km during nighttime.
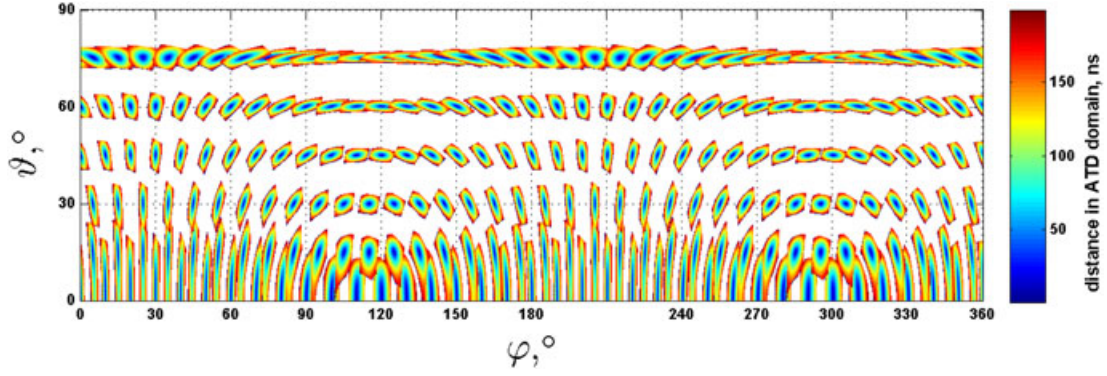
Figure 2. Resolution map of the Charmy Down network for a time difference accuracy of ∼100 ns. Solution areas are centered in regularly spaced sky points with 10° step in bearing and 15° step in elevation starting from the $(0°, 0°)$ point. Color corresponds to the distance between the sky point projection and the target point in the ATD phase space, measured in nanoseconds.

all accuracy level of the time differences is estimated to be ∼300 ns.

[17] 2. The accuracy of the minimization procedure (6) is fixed and equals 0.5°, because this procedure is evaluated on a fixed $1° \times 1°$ grid in the upper hemisphere $\mathcal{U}$ of a unit sphere. It is possible to provide any desired accuracy on this step which is only restricted by the computational costs. For the Charmy Down and Rustrel experiments, half of a degree accuracy is more than enough, because the best network's resolution is estimated to be not better than $1°$ (see below in this section).

[18] 3. The network resolution is defined by the network geometry and depends on the accuracy level of the time differences. The network of N instruments is characterized by $(N-1)$ linearly independent arrival time differences for a signal source arriving from a specific direction (φ_0, ϑ_0). All possible directions in the sky (the upper hemisphere of a unit sphere $\mathcal{U}$) form a 2-D surface in the $(N-1)$-dimensional ATD phase space. This surface can be written in the parametric form as a set of equations by use of (4) and (2):

$$t_k = \frac{1}{c}(b_{kx} \cos\varphi \cos\vartheta + b_{ky} \sin\varphi \cos\vartheta + b_{kz} \sin\vartheta), \quad k = 1, .., N-1, \tag{10}$$

where t_k is the time difference for the kth use of (4) and (2) pair, c is speed of light, (b_{kx}, b_{ky}, b_{kz}) is the kth station

pair vector and $(\varphi, \vartheta) \in \mathcal{U}$ is the direction to a source which varies over the entire sky (the upper hemisphere $\mathcal{U}$ of a unit sphere).

[19] Arrival time differences from actual measurements have a certain accuracy, e.g., for the Charmy Down experiment, 100 ns. This means that the exact time differences t_k which correspond to an exact solution always differ from the observed time differences t_{Ok} and belong to a $(N-1)$-dimensional cube in the ATD phase space:

$$| t_k - t_{Ok} | \leq \delta t_k, \quad k = 1, .., N-1, \tag{11}$$

where t_k are the cube variables, t_{Ok} is the cube center which corresponds to the set of observed time differences and δt_k is the accuracy level for the kth station pair, which is 100 ns for all pairs in the Charmy Down experiment and 300 ns in the Rustrel experiment.

[20] All physical sets of time differences that correspond to the observed set of time differences t_{Ok} within the accuracy level δt_k belong to an intersection of the cube (11) with the surface (10)

$$\left| \frac{1}{c} \left(b_{kx} \cos\varphi \cos\vartheta + b_{ky} \sin\varphi \cos\vartheta + b_{kz} \sin\vartheta \right) - t_{Ok} \right|$$
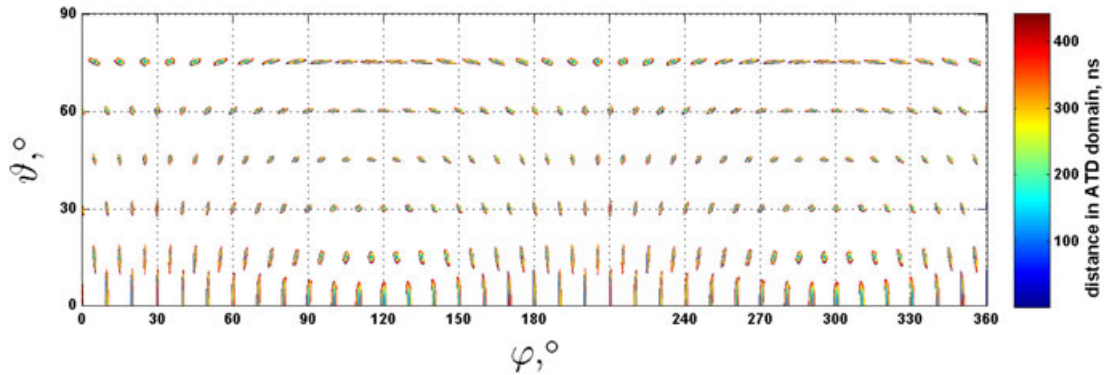$$\leq \delta t_k, \quad k = 1, .., N-1, \tag{12}$$

Figure 3. Resolution map of the Rustrel network for a time difference accuracy of ∼300 ns. Solution areas are centered in regularly spaced sky points with 10° step in bearing and 15° step in elevation starting from the $(0, 0)$ point. Color corresponds to the distance between the sky point projection and the target point in the ATD phase space, measured in nanoseconds.
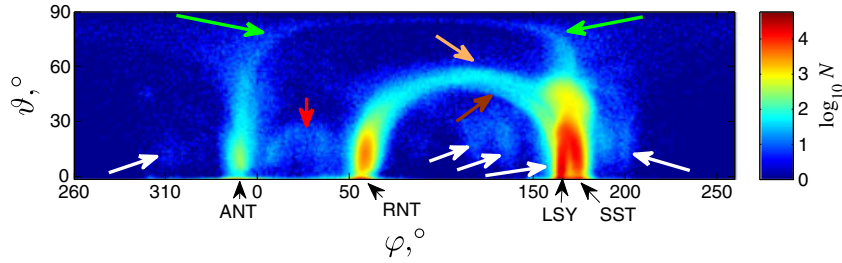
Figure 4. Map of the radio sky in the frequency range 90–110 kHz for all sources with a significant signal-to-noise ratio. Green arrows indicate LSY-ANT interference. Red, orange, and brown arrows indicate RNT-ANT, RNT-SST, and RNT-LSY interference. White arrows indicate clusters of lightning discharges.

where $(\varphi, \vartheta) \in \mathcal{U}$ varies over the entire sky (the upper hemisphere $\mathcal{U}$ of a unit sphere). This intersection defines an area in the sky where the signal with the observed time differences t_{Ok} could arrive from. The collection of such intersections of all possible cubes centered at all possible sky points $(\varphi, \vartheta) \in \mathcal{U}$ results in the resolution map of the network. This resolution map characterizes the network geometry and shows the structure of solution areas in the sky for a fixed accuracy level of the time differences.

[21] Based on this concept, the resolution maps of the Charmy Down and Rustrel networks are calculated in the following way. The solution areas are centered on regularly spaced sky points (φ_s, ϑ_s) with $10°$ steps in bearing and $15°$ steps in elevation starting from the $(0°, 0°)$ point. These sky points (φ_s, ϑ_s) correspond to the cube centers t_{Ok} in the ATD domain:

$$t_{Ok} = \frac{1}{c} \left(b_{kx} \cos \varphi_s \cos \vartheta_s + b_{ky} \sin \varphi_s \cos \vartheta_s + b_{kz} \sin \vartheta_s \right),$$
$$k = 1, .., N-1. \tag{13}$$

The solution areas are obtained by checking the conditions (12) on the entire sky (φ, ϑ) covered by the $0.1° \times 0.1°$ grid. The sky points $t_k(\varphi, \vartheta)$ (10) that belong to the solution area (12) are characterized by the distance $T(\varphi, \vartheta; \varphi_s, \vartheta_s)$ to the center of the area $t_{Ok}(\varphi_s, \vartheta_s)$ (13) in the ATD domain measured in nanoseconds:

$$T(\varphi, \vartheta; \varphi_s, \vartheta_s) = \sqrt{\sum_{k=1}^{N-1} (t_k(\varphi, \vartheta) - t_{Ok}(\varphi_s, \vartheta_s))^2}. \tag{14}$$

[22] Figure 2 shows the resolution map of the Charmy Down network for time differences with an accuracy level of 100 ns calculated by use of the described method. Color scale corresponds to the distance $T(\varphi, \vartheta; \varphi_s, \vartheta_s)$ measured in

nanoseconds. Taking $T(\varphi, \vartheta; \varphi_s, \vartheta_s) = 100$ ns as one sigma level, the resulting bearing accuracy of the network varies from $\sim 1°$ to $\sim 2°$ for the zero elevation and from $\sim 3°$ to $\sim 6°$ for $75°$ elevation. The resulting elevational accuracy varies from $\sim 10°$ to $\sim 15°$ for the zero elevation and from $\sim 1°$ to $\sim 2°$ for $75°$ elevation angle.

[23] Similarly, Figure 3 represents the resolution map of the Rustrel network calculated for time differences with an accuracy level of 300 ns. Taking $T(\varphi, \vartheta; \varphi_s, \vartheta_s) = 300$ ns as one sigma level, the resulting bearing accuracy of the network varies from $\sim 0.5°$ to $\sim 1°$ for the zero elevation and from $\sim 1.5°$ to $\sim 3°$ for $75°$ elevation. The resulting elevational accuracy varies from $\sim 6°$ to $\sim 10°$ for the zero elevation and from $\sim 0.5°$ to $\sim 1°$ for $75°$ elevation angle.

[24] The solution areas demonstrate larger extent in elevation close to the horizon, when compared to higher elevation areas. This is common for flatly distributed networks and known as the "fish eye effect" which results in the poorest resolution of the flat network in the coordinate normal to the plane of the network for the signals arriving close to that plane. The resolution map shows how the network geometry defines the structure of the radio sky image produced by the network, in which areas the network has a good or poor resolution.

[25] In practice, signals are always recorded with a certain signal-to-noise ratio. This means that a stationary transmitter appears on a radio image as an area in the sky defined by the resolution map of the network.

5. Mapping the Radio Sky

[26] The low-frequency radio sky is mapped by treating each $10\,\mu s$ long time interval of the recordings as a separate radio source, because $10\,\mu s$ corresponds to one oscillation
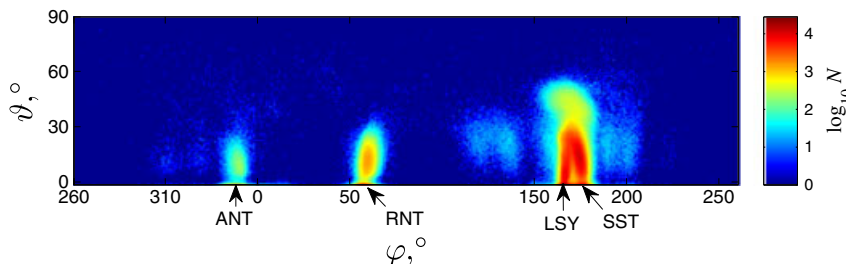

Figure 5. Map of the radio sky after exclusion of the interference between transmitters of the Lessay chain and the Sylt chain by removing the transmissions of the Sylt chain.
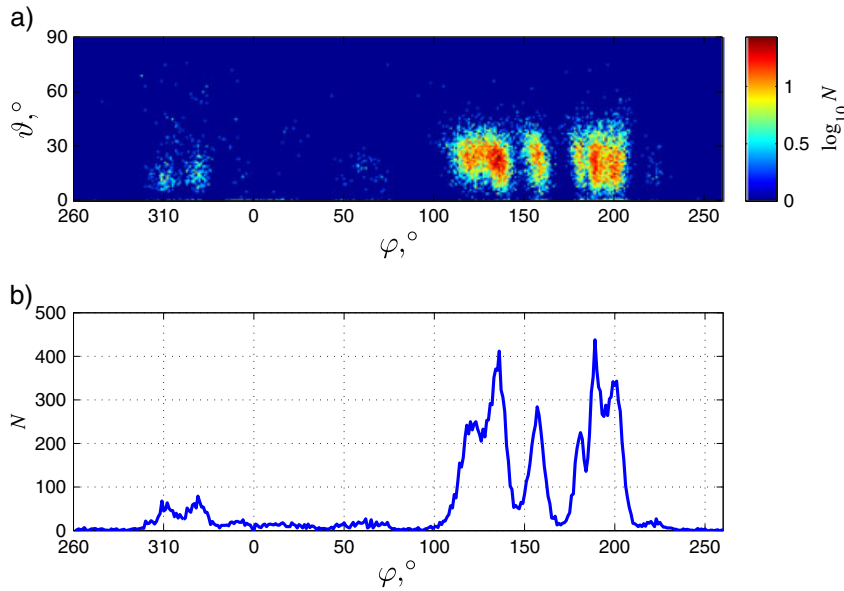
Figure 6. (a) Map of the radio sky after exclusion of all LORAN transmitters which reveals clusters of lightning discharges in thunderstorms at known locations. (b) The azimuthal distribution of lightning discharges calculated from an integration of the map over all elevation angles.

at a carrier frequency of 100 kHz. This is possible for the Charmy Down network because the longest baseline (~1.26 km) constitutes one third of the 100 kHz wavelength (~3 km) such that all instruments of the network record at least ~70% of the same 10 μs long cycle. The recordings of each 10 μs cycle are used to calculate the phase of its 100 kHz spectral component. The phase difference measured between two instruments corresponds to a time of arrival difference

$$\Delta t_k = \frac{\Delta \varphi_k}{2\pi} \cdot 10 \, \mu s. \qquad (15)$$

The time differences of nine linearly independent pairs of instruments are used for the subsequent analysis. The bearing and elevation angle are subsequently determined by the use of the theory and those experimental measurements with a significant signal-to-noise ratio recorded during the time interval from 14:36:45–14:56:45 UTC on 13 May 2011. The resulting bearings and elevations are mapped on a grid of $1° \times 1°$. The logarithm of the total number of source counts in each grid cell is used to calculate the final radio map which exhibits a rich information content (Figure 4).

[27] Several different structural elements can be discriminated. The map is dominated by the four LORAN transmitters (LSY, SST, ANT, and RNT), which can be clearly identified on the horizon. The expected and observed bearings are in excellent agreement (Table 3). The LORAN transmissions from the horizon are associated with a distortion in elevation in accordance with the resolution map (Figure 2). The size of the observed patches in the sky above the horizon corresponds to a timing accuracy of ~30 ns for LSY and ~100 ns for the other LORAN transmitters as a result of their lower signal-to-noise ratio.

[28] Another structural element on the map are the arcs in the sky which connect different LORAN transmitters. These arcs result from the interference between LORAN transmitters in different chains as described in section 3. The interchain interference can be removed by excluding the

emission times of the interfering LORAN transmitters from the Sylt chain (Figure 5), because the transmission times of LORAN transmitters are well documented.

[29] The last structural element on the radio map are diffuse clusters of radio sources in the sky. These clusters are seen more clearly when all LORAN transmissions are removed from the map (Figure 6a). Integrating the source counts over all elevation angles results in the number of
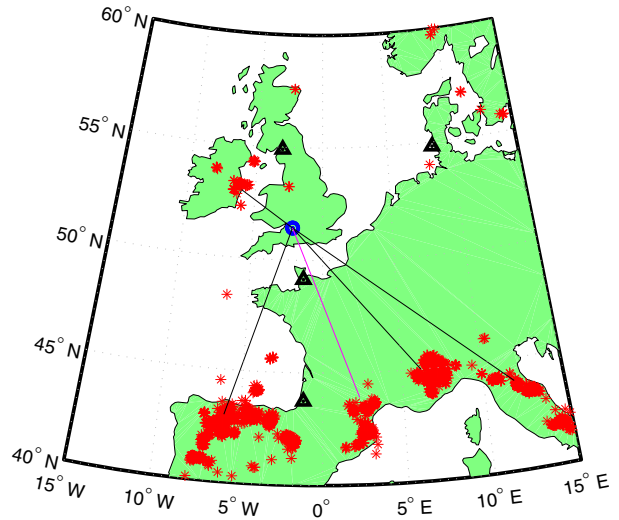

Figure 7. Relative locations of the Charmy Down network (blue circle), LORAN transmitters (black triangles), and lightning discharges (red stars) during the measurements. The bearings from the network to major thunderstorms (Figure 6) are indicated by black lines and equal 125°, 135°, 200°, and 310°. The bearing to a thunderstorm which was hidden behind the LSY transmitter is indicated by the magenta line and equals 160°.
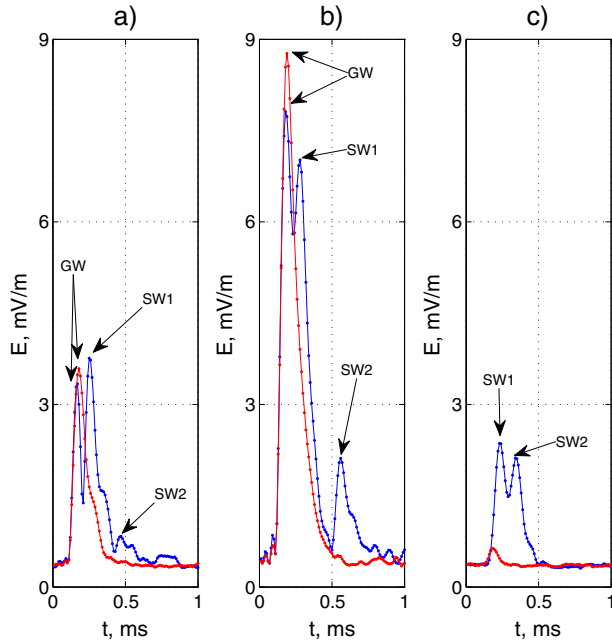
Figure 8. Examples of the demodulated waveforms of a single LORAN pulse for the LORAN transmitters (a) LSY, (b) SST, and (c) ANT recorded by the network deployed in Southern France. First and second sky hop waves are observed during the night (blue lines) while no significant sky hop waves are observed during daytime (red lines). Note that the ANT transmitter does not exhibit any significant ground wave because of the strong attenuation with distance (compare to Table 4). Ground waves are marked as GW, first hop sky waves as SW1 and second hop sky waves are denoted as SW2.

source counts depending on the bearing (Figure 6b). This distribution corresponds to the lightning activity in Europe as inferred from the lightning locations provided by the UK Met Office (Figure 7).

[30] During the Charmy Down experiment, daytime recordings were collected. The aim of this study is to demonstrate the ability of a small-scale LF network to detect signals arriving from an elevation angle well above the horizon. This aim can be achieved by using the LORAN sky hop reflections from the ionospheric D layer. However, during the daytime recordings at Charmy Down, it was impossible to observe clear sky hop waves. As a result, a second experiment was carried out with the network during the nighttime. This network was deployed over an area of $\sim 10 \times 10$ km^2 because the larger baselines increase the network resolution, based on the experience gained from the experiment in Charmy Down (this new network was deployed in Southern France on 11 August 2011). The aim of the experiment is to demonstrate the ability of the network to resolve elevation angles $\sim 10°–15°$ which are necessary for the detection of radio sources above thunderclouds at a height $\sim 50–80$ km and a distance of ~ 300 km. This aim can be achieved by analyzing the sky waves of the LORAN transmissions arriving from distinct elevation angles (Table 4).

[31] The daytime and nighttime waveforms of the three LORAN transmitters are shown in Figure 8 (RNT trans-

mitter was off that day due to maintenance works). The demodulated waveforms of the LORAN transmissions are averaged over 1 min for nighttime and daytime to increase the signal-to-noise ratio. The nighttime waveforms (blue curves) exhibit strong first and second hop sky waves which are absent during daytime (red curves) (Figure 8). The source locations of the ground and sky waves are determined by the use of the technique described in section 2, equations (5) and (6). The way to calculate the arrival time differences of the LORAN signals is a little different than the one used for the Charmy Down network because the baselines (~ 10 km) in the Rustrel experiment are longer than the wavelength (~ 3 km) and the radio signals arriving from different directions of the sky no longer belong to the same 10 µs cycles of the different instruments' recordings. Certain time shifts dependent on the instrument location and LORAN transmitter analyzed are introduced into the recordings of each instrument to compensate this 10 µs cycle mismatch. Thus, the total arrival time difference consists of this cycle correction shift which can be calculated with 1 µs precision (because the exact bearings of the LORAN transmitters are known) and the delay calculated by use of the 10 µs cycle phase difference between the two instruments (15).

[32] The resulting nighttime radio map shows the elevations of the sky waves (Figure 9), which are calculated based on the processing of the 10 µs cycles corresponding to the maxima of the ground wave and the first and second hop sky waves of the waveforms shown in Figure 8. The results agree with the expected elevations within $\sim 2°$ (Table 4). It is interesting to note that the ground wave from ANT is not present as a result of the attenuation over the large distance from the network.
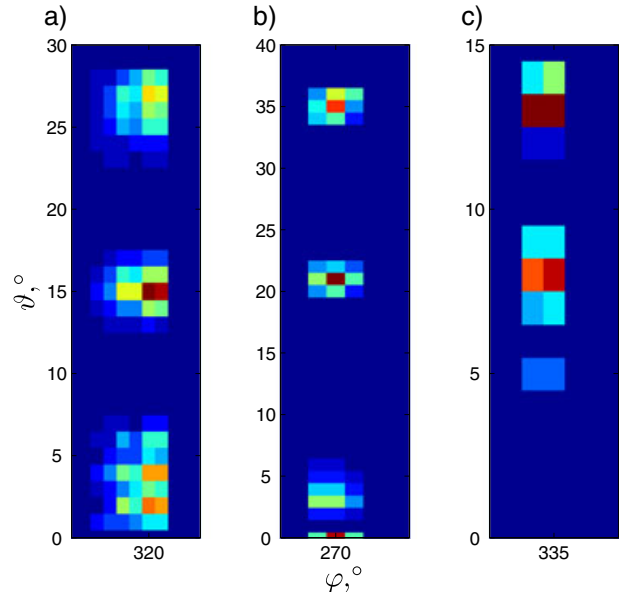

Figure 9. Locations of the ground wave and the first and second sky hop waves for the LORAN transmitters (a) LSY, (b) SST, and (c) ANT as observed with a network deployed in Southern France. Note that the ANT transmitter does not exhibit a significant ground wave because of the strong attenuation with distance (compare to Table 4).

6. Summary

[33] The design of an interferometric network of low-frequency radio receivers is described to map the 100 kHz radio sky. The design is validated with the operation of a network of instruments distributed over an area of $\sim 1 \times 1$ km^2 and $\sim 10 \times 10$ km^2. The resolution map of the network is used for a quantitative assessment of the angular resolution of the network which is important for an interpretation of the radio maps. The resulting bearing accuracy of the 1×1 km^2 (Charmy Down) network varies from $\sim 1°$ to $\sim 2°$ for 0° elevation and decreases for higher elevations varying from $\sim 3°$ to $\sim 6°$ for 75° elevation. The resulting elevational accuracy varies from $\sim 10°$ to $\sim 15°$ for 0° elevation and increases with elevation varying from $\sim 1°$ to $\sim 2°$ for 75° elevation angle. 10×10 km^2 (Rustrel) network provides better resolution because of longer baseline lengths. Its resulting bearing accuracy varies from $\sim 0.5°$ to $\sim 1°$ for zero elevation and from $\sim 1.5°$ to $\sim 3°$ for 75° elevation. The resulting elevational accuracy varies from $\sim 6°$ to $\sim 10°$ for zero elevation and from $\sim 0.5°$ to $\sim 1°$ for 75° elevation angle.

[34] Charmy Down 100 kHz radio image exhibits three main structural elements which are associated with LORAN transmitters, LORAN interchain interference and close (up to ~ 1000 km) lightning activity. The ability of the network to detect and locate the radio signals arriving from an elevation is validated with the operation of the network deployed in Rustrel, Southern France. The elevation angles of the first and second hop sky waves from LORAN transmissions are determined by the network in agreement with the expected elevation angles within $\sim 2°$ accuracy.

[35] A future application of the small-scale interferometric network is, for example, to use the network for the detection of transient events which have higher signal-to-noise ratios than LORAN transmissions because they cover a broader frequency range. On the other hand, transient events are not repetitive such that averaging is not possible to increase the signal-to-noise ratio. As a result, the resolution map for a specific network geometry defines the angular resolution for individual transient events. Such kind of data analysis could be applied in the future to the radio recordings of multihop sky waves from lightning discharges [*Shao et al.*, 2013; *Smith et al.*, 2004], relativistic electron beams above thunderclouds [*Füllekrug et al.*, 2011], and sprite streamers above thunderclouds [*Qin et al.*, 2012]. But the methodology could also be used to study the low-frequency electromagnetic radiation emanating from source regions created by HF heating of the ionosphere during the presence of auroral electroject current [*Moore et al.*, 2012] or to study in more detail the arrival of auroral kilometric radiation on the ground [*LaBelle and Anderson*, 2011].

References

Betz, H., K. Schmidt, P. Oettinger, and M. Wirz (2004), Lightning detection with 3-D discrimination of intracloud and cloud-to-ground discharges, *Geophys. Res. Lett.*, *31*, L11108, doi:10.1029/2004GL019821.

Cummer, S., and M. Füllekrug (2001), Unusually intense continuing current in lightning produces delayed mesospheric breakdown, *Geophys. Res. Lett.*, *28*(3), 495–498, doi:10.1029/2000GL012214.

Cummer, S., and U. Inan (1997), Measurement of charge transfer in sprite-producing lightning using ELF radio atmospherics, *Geophys. Res. Lett.*, *24*(14), 1731–1734, doi:10.1029/97GL51791.

Cummer, S., J. Li, F. Han, G. Lu, N. Jaugey, W. Lyons, and T. Nelson (2009), Quantification of the troposphere-to-ionosphere charge transfer in a gigantic jet, *Nat. Geosci.*, *2*, 617–620, doi:10.1038/NGEO607.

Cummins, K., M. Murphy, E. Bardo, W. Hiscox, R. Pyle, and A. Pifer (1998), A combined TOA/MDF technology upgrade of the U.S. National Lightning Detection Network, *J. Geophys. Res.*, *103*(D8), 9035–9044, doi:10.1029/98JD00153.

Dowden, R., J. Brundell, and C. Rodger (2002), VLF lightning location by time of group arrival (TOGA) at multiple sites, *J. Atmos. Sol.-Terr. Phys.*, *64*(7), 817–830, doi:10.1016/S1364-6826(02)00085-8.

Füllekrug, M. (2010), Wideband digital low-frequency radio receiver, *Meas. Sci. Technol.*, *21*, 1–9, doi:10.1088/0957-0233/21/1/015901.

Füllekrug, M., and S. Constable (2000), Global triangulation of intense lightning discharges, *Geophys. Res. Lett.*, *27*(3), 333–336, doi:10.1029/1999GL003684.

Füllekrug, M., D. Moudry, G. Dawes, and D. Sentman (2001), Mesospheric sprite current triangulation, *J. Geophys. Res.*, *106*(17), 20,189–20,194, doi:10.1029/2001JD900075.

Füllekrug, M., M. Parrot, M. Ash, I. Astin, P. Williams, and R. Talhi (2009), Transionospheric attenuation of 100 kHz radio waves inferred from satellite and ground based observations, *Geophys. Res. Lett.*, *36*, L06104, doi:10.1029/2008GL036988.

Füllekrug, M., R. Roussel-Dupré, M. Symbalisty, O. Chanrion, A. Odzimek, O. van der Velde, and T. Neubert (2010), Relativistic runaway breakdown in low frequency radio, *J. Geophys. Res.*, *115*, A00E09, doi:10.1029/2009JA014468.

Füllekrug, M., et al. (2011), Relativistic electron beams above thunderclouds, *Atmos. Chem. Phys.*, *11*, 7747–7754, doi:10.5194/acp-11-7747-2011.

Füllekrug, M., et al. (2013), Energetic charged particles above thunderclouds, *Surv. Geophys.*, *34*, 1–41, doi:10.1007/s10712-012-9205-z.

Gemelos, E., U. Inan, M. Walt, M. Parrot, and J. Sauvaud (2009), Seasonal dependence of energetic electron precipitation: Evidence for a global role of lightning, *Geophys. Res. Lett.*, *36*, 1–5, doi:10.1029/2009GL040396.

Inan, U., D. Piddyachiy, W. Peter, J. Sauvaud, and M. Parrot (2007), DEMETER satellite observations of lightning-induced electron precipitation, *Geophys. Res. Lett.*, *34*, L07103, doi:10.1029/2006GL029238.

Krehbiel, P., J. Riousset, V. Pasko, R. Thomas, W. Rison, M. Stanley, and H. Edens (2008), Upward electrical discharges from thunderstorms, *Nat. Geosci.*, *1*, 233–237, doi:10.1038/ngeo162.

LaBelle, J., and R. Anderson (2011), Ground level detection of auroral kilometric radiation, *Geophys. Res. Lett.*, *38*, 1–4, doi:10.1029/2010GL046411.

Lee, A. (1986), An experimental study of the remote location of lightning flashes using a VLF arrival time difference technique, *Q. J. Roy. Meteor. Soc.*, *112*, 203–229, doi:10.1002/qj.49711247112.

Lewis, E. A., R. B. Harvey, and J. E. Rasmussen (1960), Hyperbolic direction finding with sferics of transatlantic origin, *J. Geophys. Res.*, *65*(7), 1879–1905.

Moore, R., S. Fujimaru, M. Cohen, M. Gokowski, and M. McCarrick (2012), On the altitude of the ELF/VLF source region generated during beat-wave HF heating experiments, *J. Geophys. Res.*, *39*, L18101, doi:10.1029/2012GL053210.

Pasko, V., U. Inan, T. Bell, and S. Reising (1998), Mechanism of ELF radiation from sprites, *Geophys. Res. Lett.*, *25*(18), 3493–3496, doi:10.1029/98GL02631.

Qin, J., S. Celestin, and V. Pasko (2012), Low frequency electromagnetic radiation from sprite streamers, *Geophys. Res. Lett.*, *39*, L22803, doi:10.1029/2012GL053991.

Rodger, C., S. Werner, J. Brundell, E. Lay, N. Thomson, R. Holzworth, and R. Dowden (2006), Detection efficiency of the VLF World-Wide Lightning Location Network (WWLLN): Initial case study, *Ann. Geophys.*, *24*, 3197–3214, doi:10.5194/angeo-24-3197-2006.

Rodger, C., C. Enell, E. Turunen, M. Clilverd, N. Thomson, and P. Verronen (2007), Lightning-driven inner radiation belt energy deposition into the atmosphere: Implications for ionisation-levels and neutral chemistry, *Ann. Geophys.*, *25*, 1745–1757, doi:10.5194/angeo-25-1745-2007.

Roussel-Dupré, R., E. Symbalisty, Y. Taranenko, and V. Yukhimuk (1998), Simulations of high-altitude discharges initiated by runaway break-

down, *J. Atmos. Sol.-Terr. Phys.*, *60*, 917–940, doi:10.1016/S1364-6826(98)00028-5.

Said, R., U. Inan, and K. Cummins (2010), Long-range lightning geolocation using a VLF radio atmospheric waveform bank, *J. Geophys. Res.*, *115*, D23108, doi:10.1029/2010JD13863.

Sato, M., and H. Fukunishi (2003), Global sprite occurrence locations and rates derived from triangulation of transient Schumann resonance events, *Geophys. Res. Lett.*, *30*(16), 1859–1862, doi:10.1029/2003GL017291.

Shao, X., M. Stanley, A. Regan, J. Harlin, M. Pongratz, and M. Stock (2006), Total lightning observations with the new and improved Los Alamos Sferic Array (LASA), *J. Atmos. Ocean Tech.*, *23*, 1273–1288, doi:10.1175/JTECH1908.1.

Shao, X., E. Lay, and A. Jacobson (2013), Reduction of electron density in the night-time lower ionosphere in response to a thunderstorm, *Nat. Geosci.*, *6*, 29–33, doi:10.1038/NGEO1668.

Smith, D., M. Heavner, A. Jacobson, X. Shao, R. Massey, R. Sheldon, and K. Wiens (2004), A method for determining intracloud lightning and ionospheric heights from VLF/LF electric field records, *Radio Sci.*, *39*, RS1010, doi:10.1029/2002RS002790.

United States Coast Guard (1994), Specification of the transmitted LORAN-C signal. COMDTINST M16562.4A, Washington D. C.